Article

Rapid Quantification of Tissue Perfusion Properties with a Two-Stage Look-Up Table

Bin Yang

Department of Engineering, Duquesne University, Pittsburgh, PA 15282, USA; yangb1@duq.edu

Abstract: Tissue perfusion properties reveal crucial information pertinent to clinical diagnosis and treatment. Multispectral spatial frequency domain imaging (SFDI) is an emerging imaging technique that has been widely used to quantify tissue perfusion properties. However, slow processing speed limits its usefulness in real-time imaging applications. In this study, we present a two-stage look-up table (LUT) approach that accurately and rapidly quantifies optical (absorption and reduced scattering maps) and perfusion (total hemoglobin and oxygen saturation maps) properties using stage-1 and stage-2 LUTs, respectively, based on reflectance images at 660 and 850 nm. The two-stage LUT can be implemented on both CPU and GPU computing platforms. Quantifying tissue perfusion properties using the simulated diffuse reflectance images, we achieved a quantification speed of 266, 174, and 74 frames per second for three image sizes 512×512, 1024×1024, and 2048×2048 pixels, respectively. Quantification of tissue perfusion properties was highly accurate with only 3.5% and 2.5% error for total hemoglobin and oxygen saturation quantification, respectively. The two-stage LUT has the potential to be integrated with dual-sensor cameras to enable real-time quantification of tissue hemodynamics.

Keywords: spatial frequency domain imaging; hemodynamics; perfusion properties; Monte Carlo simulation; look-up table

1. Introduction

Sufficient oxygen supply in tissue is critical to maintaining its normal physiological functions [1,2]. Local oxygen levels in tissue provide valuable insights into its health states, such as metabolic levels [3]. Oxygen is transported via binding to hemoglobin, the main protein of red blood cells, to different parts of the body, and is released to tissue through perfusion. Depending on the presence of binding oxygen molecules, hemoglobin can exist in two forms, oxygenated and deoxygenated hemoglobin, both of which exhibit distinct absorption properties in visible and near-infrared (NIR) ranges. Based on the differential absorption of hemoglobin, multispectral imaging was developed to quantify tissue perfusion properties, such as oxygen saturation [4]. However, the quantification accuracy was limited due to its inability to decouple tissue absorption from tissue scattering. Spatial frequency domain imaging (SFDI), on the other hand, independently evaluates tissue absorption and scattering properties [5–7]. SFDI uses 2D sinusoidal structured illumination to interrogate the samples. Tissue absorption and scattering modify the modulation of the illumination, and diffuse reflectance thus encodes the tissue's optical properties. To quantify tissue optical properties, typically, a set of three 2D sinusoidal patterns with a phase shift of 0°, 120°, and 240° are projected onto the sample surfaces sequentially, and corresponding images are acquired. Using the 3-phase demodulation technique, two images, often referred as AC and DC images, are derived. AC and DC images are calibrated to obtain modulation and reflectance images, which serve as searching indices of the pre-generated look-up tables (LUTs) to determine optical properties of the sample. Multispectral SFDI has been developed to map perfusion and hemodynamic properties of the tissue with an improved accuracy [8,9]. Such quantification requires

imaging at multiple wavelengths (two wavelengths at least), typically in the red and near-infrared (NIR) range [10,11]. At each wavelength, a set of three phase-shifted patterns are projected onto the tissue surface and the corresponding reflectance images are acquired to determine the tissue's optical and perfusion properties [6].

The overall process, however, is slow and limits the temporal resolution. In the past few years, significant efforts have been devoted to improving the imaging and quantification speed in SFDI imaging. Single snapshot SFDI reduced the number of required images from three to one [12–14], and look-up table (LUT)-based quantification significantly improved the quantification speed of optical property of the tissue [15]. For perfusion property quantification, the Beer–Lambert Law is the standard approach, which, however, can be slow for large images. To improve the speed for perfusion property quantification, artificial intelligence has been employed to train the predictive model based on a large set of training images [16,17].

Despite recent advancements towards real-time mapping of tissue perfusion and hemodynamics, current methods are still limited by relatively slow processing speed, low image resolution, and the need for powerful computational hardware (e.g., a multi-GPU setup). This study aimed to develop a highly efficient LUT-based computational framework towards high-resolution real-time mapping of tissue perfusion and hemodynamics that can be implemented on cost-effective hardware platforms.

2. Materials and Methods

LUT techniques have been widely used in SFDI to determine optical properties without performing time-consuming fitting procedures [18]. However, LUT techniques are rarely used to quantify tissue perfusion properties in conjunction with SFDI imaging. In this study, we developed a highly efficient two-stage LUT technique consisting of two connected LUTs. The first and second stage LUTs rapidly quantify tissue optical and perfusion properties, respectively. Figure 1 summarizes the overall workflow of the two-stage LUT technique.
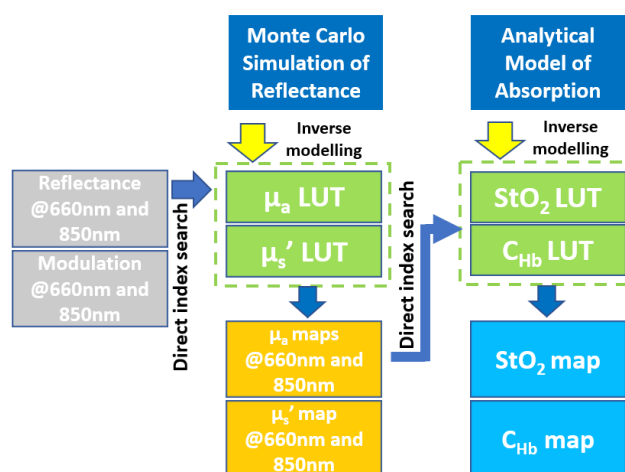

Figure 1. Overview of two-stage LUT. Monte Carlo simulation of reflectance and an analytical model of blood absorption are inverted to generate LUTs for optical property mapping (stage-1) and perfusion mapping (stage-2), respectively. SFDI measurements at 660 and 850 nm are used as inputs to quantify absorption and reduced scattering coefficients. The absorption coefficients are later used as search indices to quantify oxygen saturation and total hemoglobin concentration.

The stage-1 LUT was generated by inverse modeling diffuse reflectance obtained by Monte Carlo simulation in the spatial frequency domain, and the stage-2 LUT was generated by inverse modeling of an analytical model of tissue absorption. Quantification of tissue perfusion properties was based on SFDI imaging at 660 and 850 nm. These two wavelengths located on the opposite side of the isosbestic wavelength, around 800 nm, have been previously demonstrated to effectively quantify blood perfusion properties [16]. With

the two-stage LUT, reflectance and modulation measurements at both 660 and 850 nm were first used as search indices to determine absorption and reduced scattering coefficients using the stage-1 LUT. The absorption coefficients at 660 and 850 nm were subsequently used as searching indices to efficiently determine oxygen saturation and blood concentration using the stage-2 LUT. In the rest of this section, detailed procedures for generating and evaluating the performance of two-stage LUT for quantifying perfusion properties are presented.

2.1. Stage-1 LUT for Quantifying Optical Properties

Monte Carlo (MC) simulation has been widely used for simulating light transport in turbid media. The simulation results are often used to generate LUTs for quantifying optical properties through inverse modeling [19,20]. Traditionally, MC simulation was implemented on a CPU [21], and is considered computationally intensive and slow [22]. Due to its highly parallel nature of execution, graphic computing unit (GPU)-based MC simulation programs have recently been developed, which significantly improve the simulation efficiency [23]. This study adopted the Monte Carlo eXtreme (MCX) simulation package developed by Fang and Boas to simulate reflectance in the spatial frequency domain [24].

We simulated reflectance images under structured illumination with a spatial frequency of 0.125 mm^{-1} on large virtual phantoms (9.6 cm $\times$ 9.6 cm $\times$ 5 cm) with a grid size of 0.1 mm in the x, y, and z directions. The sample thickness of 5 cm was chosen to satisfy the requirement for infinite geometry in MC simulations [18]. To reflect the general properties of biological tissue, the virtual phantom was assumed to have an anisotropy g = 0.9 and a refractive index n = 1.37 [25]. A total of 208 pairs of biologically relevant optical properties were simulated with 16 absorption coefficient (μ_a) values from 0.001 to 1 mm^{-1}, and 13 reduced scattering coefficient values (μ_s') from 0.5 to 3 mm^{-1}. For each sample, diffuse reflectance images were simulated under 3 phase-stepped (0°, 120°, and 240°) structured illuminations. Thus, a total of 624 MC simulations were performed, and the corresponding reflectance images were saved. The MCX program assumes that one unit of energy (for example, 1 J) is deposited/launched into the medium. The simulation returns the detected optical energy density at the surface. The reflectance image was then calculated by normalizing the detected optical energy density at the surface to the incident optical energy density. Based on our analysis (data not shown), a total of 200 million photons were used in each simulation, which resulted in flat AC and DC reflectance profiles with low levels of noise (example shown in Figure 2C). It is worth noting that MCX simulation is not based on the white Monte Carlo approach; rather, each simulation is based on the actual optical properties of the medium.

Following the simulation, a sub-region of size 2.5 cm $\times$ 2.5 cm (red-dash square in Figure 2A) of each reflectance image was isolated to reduce the signal fall-off toward the edge of the image. The resultant diffuse reflectance image was then averaged along the pattern direction (yellow arrows in Figure 2A) to further improve the signal quality. Three intensity profiles, I_1, I_2, and I_3, were obtained for three phase-stepped illuminations (Figure 2B). The demodulation process shown in Equations (1) and (2) was then performed to extract DC (I_{DC}) and AC (I_{AC}) signals (Figure 2C).

$$I_{DC} = {}^1\!/_3(I_1 + I_2 + I_3) \tag{1}$$

$$I_{AC} = {}^{\sqrt{2}}\!/_3\sqrt{(I_1 - I_2)^2 + (I_2 - I_3)^2 + (I_3 - I_1)^2} \tag{2}$$

I_{DC} and I_{AC} signals were further converted to reflectance (R) and modulation (M) with Equations (3) and (4), respectively. The definitions of reflectance and modulation followed the convention that was initially introduced by Erickson et al. [18]. It is worth noting that MC simulation generates normalized reflectance images; thus, no normalization to a spectralon image is needed.
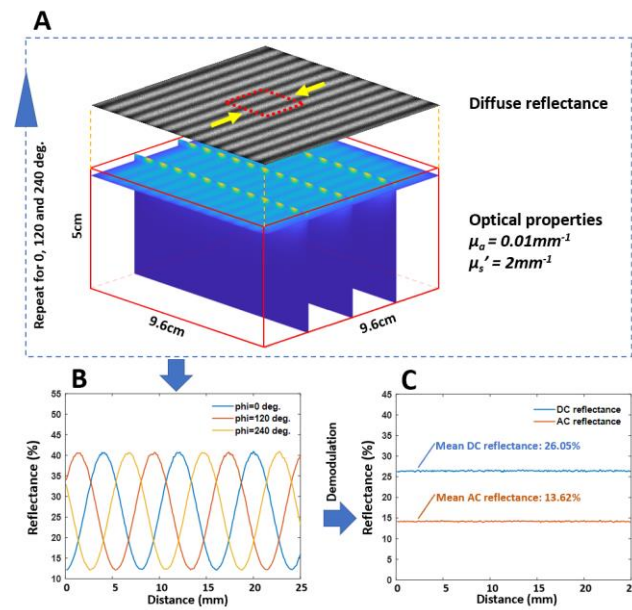
Figure 2. Monte Carlo simulation workflow. (**A**). Schematic of Monte Carlo simulation over a large volume. For each setting, the simulation was performed with phase shifts of 0, 120, and 240 degrees. The central region (red dash box) of the diffuse reflectance image (gray-scale image) was averaged along the direction of yellow arrows to obtain reflectance plots. (**B**). Reflectance plots at three phase shifts. (**C**). Demodulated AC and DC intensity plots.

$$R(\mu_a, \mu_s') = I_{DC}(\mu_a, \mu_s') \tag{3}$$

$$M(\mu_a, \mu_s') = \frac{I_{AC}(\mu_a, \mu_s')}{I_{DC}(\mu_a, \mu_s')} \tag{4}$$

Maps of $R(\mu_a, \mu_s')$ and $M(\mu_a, \mu_s')$ were converted to LUTs, $\mu_a(R, M)$ and $\mu_s'(R, M)$, using a coordinate mapping technique similar to the one described elsewhere [15]. Interested readers may refer to Figure 1 in the reference [15] for the key steps involved in the LUT generation. Briefly, after obtaining $R(\mu_a, \mu_s')$ and $M(\mu_a, \mu_s')$ from the simulation, a 2D interpolation was performed to generate another set of R and M maps with a finer and uniform grid size of μ_a and μ_s'. Data points in the newly generated $R(\mu_a, \mu_s')$ and $M(\mu_a, \mu_s')$ maps were directly mapped to generate two new maps $\mu_a(R, M)$ and $\mu_s'(R, M)$. A scattered data interpolation was used to fill the gaps in $\mu_a(R, M)$ and $\mu_s'(R, M)$ maps. To facilitate a rapid search for optical properties, during the LUT generation, reflectance and modulation were up-scaled by a factor of 1000, and rounded to the nearest integer. This operation allowed for direct index searching based on reflectance measurements.

2.2. Stage-2 LUT for Quantifying Perfusion Properties

We performed forward modeling of tissue absorption at two wavelengths, 660 and 850 nm. Hemoglobin concentration, *CHb*, was varied from 0.075 to 22.5 g/L with an increment of 0.075 g/L, which corresponds to 0.05% and 15% of the total hemoglobin concentration of 150 g/L in the whole blood. This *CHb* range reflects the majority types of organs except for the kidney, the liver, and the exposed vasculature [25]. *CHb* in those tissues is well above 30% [25]. The range of the optical and physiological properties may need to be expanded before the two-stage LUT method can be applied to characterize those tissues. Oxygen saturation, *StO*2, was varied from 50% to 100% with an increment of 0.25%. A hemoglobin molecular weight of 64,500 g/mol was used in the simulation [26]. The absorption coefficient at both wavelengths can be analytically described by Equations (5) and (6), respectively, where ε_{HbO_2} and ε_{Hb} are molar extinction coefficients of oxygenated and deoxygenated hemoglobin. The values of the molar extinction coefficients were obtained from the tabulated data compiled by Dr. Scott Prahl [27]. With a similar technique described in

the previous section, maps of $\mu_{a\_660}(StO2, CHb)$ and $\mu_{a\_850}(StO2, CHb)$ were converted to maps of $StO2(\mu_{a\_660}, \mu_{a\_850})$ and $CHb(\mu_{a\_660}, \mu_{a\_850})$, and a scaling factor of 5000 was used.

$$\mu_{a\_660}(StO2, CHb) = \frac{\log(10)}{64500}\left[\varepsilon_{HbO_2\_660} \cdot StO2 \cdot CHb + \varepsilon_{Hb\_660} \cdot (1 - StO2) \cdot CHb)\right] \quad (5)$$

$$\mu_{a\_850}(StO2, CHb) = \frac{\log(10)}{64500}\left[\varepsilon_{HbO_2\_850} \cdot StO2 \cdot CHb + \varepsilon_{Hb\_850} \cdot (1 - StO2) \cdot CHb)\right] \quad (6)$$

2.3. Quantification Speed Test

The speed of quantifying optical and perfusion properties using the two-stage LUT was evaluated based on a set of simulated diffuse reflectance images (Sections 2.3.1 and 2.3.2). The performance of the stage-2 LUT was compared to the Beer–Lambert Law-based quantification (Section 2.3.3). All quantification methods were implemented on both a CPU and GPU to fully evaluate their efficiency. GPU acceleration was achieved by simply converting a regular MATLAB array into a GPU-compatible array with the MATLAB function gpuArray(). The testing platform consisted of an Intel CPU (i9 10900K), 32 GB of memory, and a Nvidia GPU (RTX 3080). A speed test script was written in MATLAB, and only the built-in MATLAB functions were used. We performed a speed test on three sets of simulated images with resolutions of 512 × 512 pixels, 1024 × 1024 pixels, and 2048 × 2048 pixels. Each set of images consisted of 50 images. The three image sizes are later referred to as small, medium, and large sizes, respectively.

2.3.1. Optical Property Mapping Using Stage-1 LUT

Reflectance and modulation values are in the range of 0 and 1, and search indices of the LUT are integers. To enable the use of reflectance and modulation as search indices in the LUT, these values were up-scaled by a factor of 1000, and rounded to the nearest integer. This scaling factor ensures rapid and accurate determination of optical properties without making very large LUTs. The MATLAB function sub2ind() was used to convert 2D maps of scaled reflectance and modulation into linear search indices for stage-1 LUT to quantify optical properties.

2.3.2. Perfusion Property Mapping Using Stage-2 LUT

Following optical property quantification, absorption coefficient maps at 660 and 850 nm were multiplied by a scaling factor of 5000 under a similar consideration described in Section 2.3.1, and similarly, the integer portion of the result was retained. MATLAB function sub2ind() was used to convert 2D maps of scaled absorption coefficient maps into linear search indices for the stage-2 LUT to quantify perfusion properties.

2.3.3. Perfusion Property Mapping Using Beer-Lambert Law

Equations (5) and (6) were solved for concentration of oxygenated hemoglobin (=$StO2 \cdot CHb$) and deoxygenated hemoglobin (=$(1 - StO2) \cdot CHb$), based on which oxygen saturation and total hemoglobin concentration were determined. To improve the computation efficiency, 2D absorption maps were first converted to a 1D array to take advantage of the high efficiency of vectorized computation in MATLAB.

2.4. In Silico Validation

We examined the quantification accuracy of the perfusion parameters through an in silico validation procedure (Figure 3). We generated a total of 30 digital phantoms, and each phantom was characterized by the total hemoglobin concentration and oxygen saturation. Thirty phantoms were divided into 5 sets, with 6 individual phantoms in each set. The hemoglobin concentration was increased from 2.25 to 20.15 g/L with an increment of 4.5 g/L from set 1 to set 5. In each set, the oxygen saturation levels were increased from 50% to 100% with an increment of 10% for 6 phantoms. Absorption coefficients at 660 and 850 nm were calculated based on the total hemoglobin concentration and oxygen

saturation using Equations (5) and (6) for all phantoms. The absorption coefficients at both wavelengths were used to quantify hemoglobin concentration and oxygen saturation using the stage-2 LUT. The quantified hemodynamic properties were compared to the designed hemodynamic properties to assess the quantification accuracy.
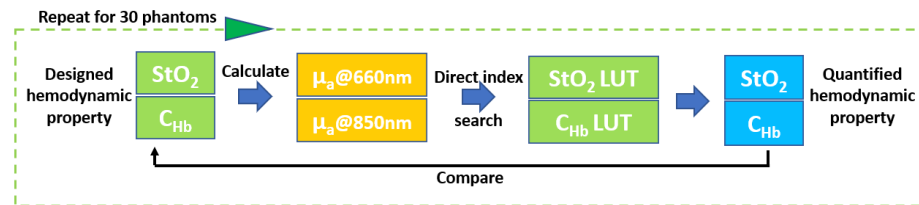

Figure 3. Flowchart of in silico quantification and validation of 30 digital phantoms.

3. Results

3.1. Two-Stage LUT

Figure 4 exhibits a two-stage LUT for optical and perfusion property mapping. The axes of each LUT are characterized by actual values and their corresponding search indices. In both stages, the corresponding search indices are used to determine the optical and perfusion properties.
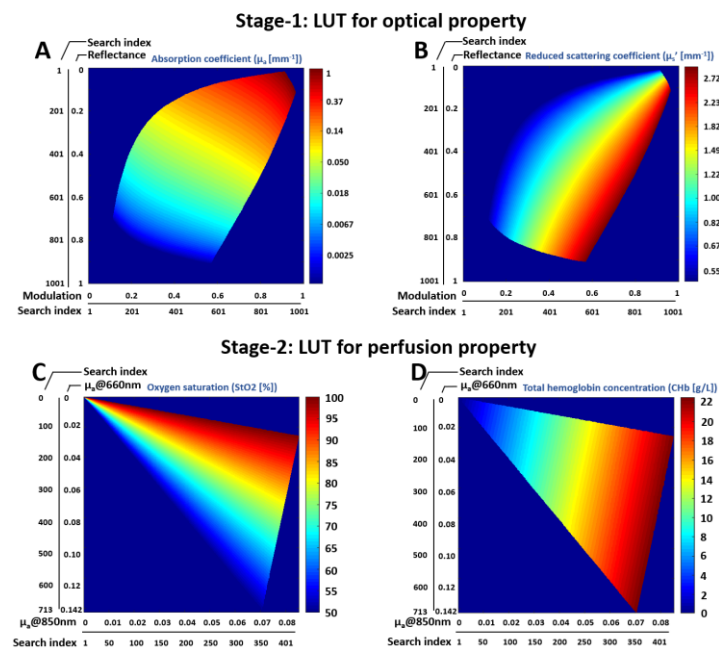

Figure 4. Two-stage LUTs for stage-1 optical (**A**,**B**) and stage-2 perfusion (**C**,**D**) property mapping. Reflectance and modulation in the stage-1 LUT, and absorption coefficients at 660 and 850 nm in the stage-2 LUT, were converted into search indices.

3.2. Quantification Speed Test

Table 1 summarizes the processing time for quantifying optical properties and perfusion properties using both GPU- and CPU-based computation. It is clear that with the GPU acceleration, the processing time of three types of quantification were reduced. Note that the LUT access time (processing time in the parentheses) accounts for a smaller portion of the overall processing time in GPU-based processing than that in CPU-based processing.

Table 1. Processing time for optical and perfusion property quantification with a GPU and CPU.

		GPU-Based			CPU-Based		
Image size (*pixels × pixels*)		512 (S)	1024 (M)	2048 (L)	512 (S)	1024 (M)	2048 (L)
Processing time (ms)	**I.** μ_a *and* μ_s' *mapping at 660 nm and 850 nm with* **stage-1 LUT**	2.36 (0.87) *	3.39 (1.04)	6.94 (2.47)	10.64 (8.19)	41.72 (31.05)	170.34 (128.84)
	II. *StO2 and CHb mapping with* **stage-2 LUT**	1.41 (0.19)	2.34 (0.22)	6.49 (0.36)	4.87 (2.69)	20.52 (10.84)	86.61 (45.96)
	III. *StO2 and CHb mapping using* **Beer-Lambert Law**	9.18	24.72	93.33	9.48	37.91	165.81

* GPU access time.

Although the quantifications for the perfusion property with both the stage-2 LUT and the Beer–Lambert Law were accelerated with a GPU, the stage-2 LUT clearly showed a much higher efficiency. The stage-2 LUT is approximately 5.5 and 13.5 times faster for small and large sized images, respectively. Without GPU acceleration, the stage-2 LUT still showed about 90% higher efficiency than the Beer–Lambert Law method.

It is worth noting that a large image size imposes a much higher penalty on CPU-based processing than on GPU-based processing. The CPU-based processing time is proportional ($1\times$, $4\times$, and $16\times$) to the image sizes for all three types of quantifications. On the other hand, the GPU-based processing time is less affected by the image sizes, especially for the LUT-based quantifications

Converting the processing time to processing speed (frames per second/FPS) revealed the GPU-based two-stage LUT (sum of processing time I and II) was capable of achieving a processing speed of 266, 174, and 74 FPS for small, median, and large sized images, respectively, which is 2.1, 3.9, and 6.5 times faster than that of the Beer–Lambert Law-based processing (sum of processing time I and III) (Figure 5A). On the other hand, CPU-based quantification was slower, but it still achieved approximately 65, 16, and 4 FPS with the two-stage LUT for three image sizes, which is about 30% faster than Beer–Lambert Law-based processing (Figure 5B).
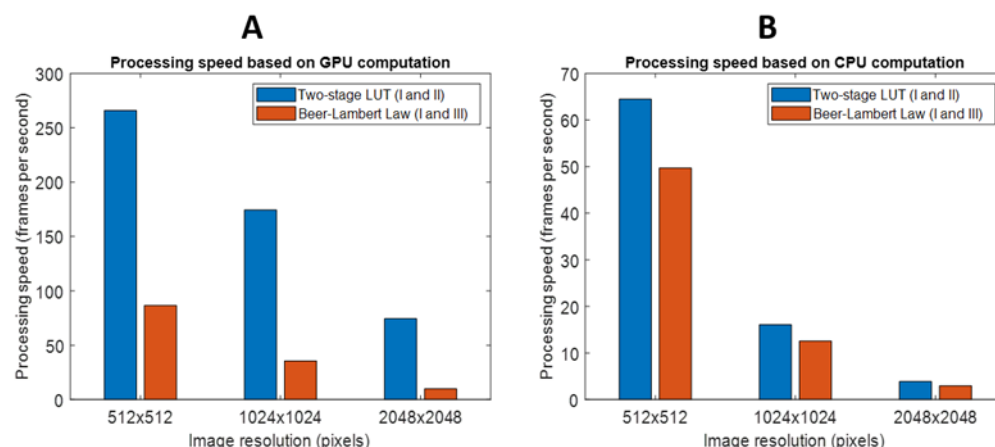

Figure 5. (**A**). Quantification frame rate of optical and perfusion properties of three image sizes with a GPU and a CPU. (**B**). Processing time increases as the image size increases for both GPU- and CPU-based processing. However, the GPU-based processing is less affected.

3.3. In-Silico Validation

The stage-2 LUT exhibited a high accuracy of quantifying perfusion properties as shown in Figure 6. The absolute quantification error is less than 3.5% for total hemoglobin concentration and less than 2.5% for oxygen saturation over a wide range of perfusion properties. Although the overall error is small, Figure 6 suggests that a lower total hemoglobin concentration may correlate with a higher error. It is worth noting that the hemodynamic

properties obtained with the Beer–Lambert Law were determined analytically, and were identical to the designed values, as it was a direct inversion of the process of calculating μ_{a_660} and μ_{a_850} shown in Equations (5) and (6).
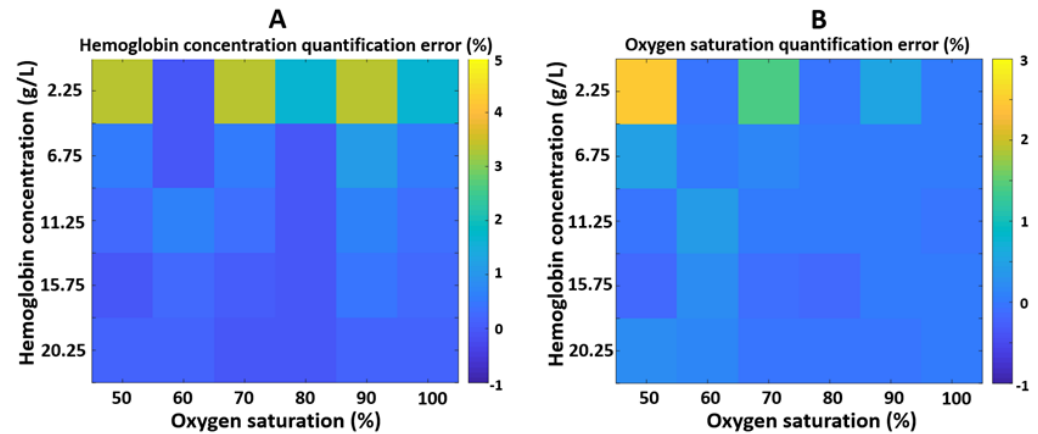

Figure 6. Relative quantification error of (**A**) total hemoglobin concentration and (**B**) oxygen saturation between the designed values and the values obtained with the stage-2 LUT.

4. Discussion

In this study, we developed and demonstrated a highly efficient and accurate two-stage LUT method that quantifies the tissue's optical and perfusion properties with SFDI. High efficiency was achieved through direct index searching of two LUTs, which eliminated time-consuming fitting operations to determine optical and, subsequently, perfusion properties. GPU-based implementation significantly improved the searching speed through parallelization. At an image size of 2048×2048 pixels, we achieved a quantification speed of 74 FPS for both optical and perfusion properties.

In recent years, methods for direct quantification of optical and perfusion properties using artificial intelligence have been reported to improve the processing speed towards real-time applications. Zhao et al. reported a processing time of 94.4 ms (excluding time for image import and result display) for quantifying perfusion properties for images with a size of 540×720 pixels using a deep residual network [17]. Using adversarial deep learning, Chen and Durr reported that approximately 40 ms was needed to determine optical and perfusion properties for images with a size of 512×512 pixels [16]. It is worth noting that both studies utilized two wavelengths at around 660 and 850 nm, which are the same wavelengths as those used in this study.

A two-stage LUT method is highly suitable for real-time applications. With GPU acceleration, it achieved 266 and 74 FPS for small and large sized images. The short processing time can provide ample room to accommodate more sophisticated algorithms while still maintaining real-time performance. When the two-stage LUT is coupled with a dual-sensor SFDI imaging system, reflectance images at 660 and 850 nm can be acquired simultaneously and processed rapidly, which would enable time-sensitive imaging applications, such as real-time tissue viability monitoring.

Two-stage LUTs outperformed the Beer–Lambert Law-based quantification regardless of the computational platform. Even with GPU acceleration, the Beer–Lambert Law method only achieved 35.5 FPS for medium sized images. Any additional processing would slow it down to sub-30 FPS, which is not ideal for real-time applications.

Although CPU-based implementation of two-stage LUT is not as fast, it does not require a dedicated GPU and offers a few advantages. First, the two-stage LUT is still suitable for offline applications where processing time is not a critical factor, and it is about 30% more efficient than the Beer–Lambert Law approach. Second, the two-stage LUT offered a processing speed of approximately 65 FPS for small sized images, which still could enable real-time applications when the image resolution is not a concern. It is worth noting that,

in real-life applications, acquiring and transferring images to memory, and displaying the processed results, take additional time. To preserve the high performance of the two-stage LUT, a multi-threaded architecture could be adopted. Each thread runs independently and is only responsible for its own task, such as image transfer, quantification, or result display.

The two-stage LUT quantification method presented in this study was intended to serve as a general framework to map the optical and perfusion properties of the tissue. Implementing this general framework requires additional considerations. Firstly, the optical property LUT was generated using MC simulation on homogenous phantoms. Homogenous phantom models have been widely used to generate LUTs for quantifying optical and physiological properties, and have yielded encouraging results. However, it is worth noting that building LUTs based on a more complex geometry, such as two-layer models, could further improve the accuracy and specificity of the quantification. Secondly, although MC simulation is highly accurate, the LUT is not imaging system-specific. When applying this LUT to quantify optical properties of the sample imaged with a specific SFDI system, additional calibration and scaling of the LUT are likely needed to match the characteristics of the imaging system and to achieve a high quantification accuracy. Thirdly, the sample's 3D surface shape affects the diffuse reflectance, and thus the quantification, which was not accounted for in our method. Multiple techniques have been reported to correct for surface height, and these methods could be adopted to improve quantification accuracy [13,28]. Finally, the two-stage LUT was based on two wavelengths that are sensitive to oxygenated and deoxygenated hemoglobin. If the tissue to be measured presents additional major chromophores, such as melanin, this method may not yield a high quantification accuracy. Higher-dimensional (e.g., three-dimensional) LUTs could be generated to account for additional chromophores.

5. Conclusions

In this work, we presented a highly efficient method, a two-stage LUT, that quantifies the tissue's optical and perfusion properties in SFDI imaging. Both GPU- and CPU-based implementations demonstrated a high efficiency. This method can potentially be adapted and incorporated into existing SFDI imaging applications to improve data processing efficiency. In future work, we will implement this two-stage LUT in a dual-wavelength SFDI imaging system to monitor tissue perfusion and hemodynamics in real time.

References

1. Ndubuizu, O.; LaManna, J.C. Brain tissue oxygen concentration measurements. *Antioxid. Redox Signal.* **2007**, *9*, 1207–1220. [CrossRef] [PubMed]
2. Boushel, R.; Langberg, H.; Olesen, J.; Gonzales-Alonzo, J.; Bülow, J.; Kjaer, M. Monitoring tissue oxygen availability with near infrared spectroscopy (NIRS) in health and disease. *Scand. J. Med. Sci. Sports* **2001**, *11*, 213–222. [CrossRef] [PubMed]
3. Rajaram, N.; Reesor, A.F.; Mulvey, C.S.; Frees, A.E.; Ramanujam, N. Non-invasive, simultaneous quantification of vascular oxygenation and glucose uptake in tissue. *PLoS ONE* **2015**, *10*, e0117132. [CrossRef] [PubMed]
4. Zuzak, K.J.; Schaeberle, M.D.; Lewis, E.N.; Levin, I.W. Visible reflectance hyperspectral imaging: Characterization of a noninvasive, in vivo system for determining tissue perfusion. *Anal. Chem.* **2002**, *74*, 2021–2028. [CrossRef] [PubMed]

5. Cuccia, D.J.; Bevilacqua, F.; Durkin, A.J.; Tromberg, B.J. Modulated imaging: Quantitative analysis and tomography of turbid media in the spatial-frequency domain. *Opt. Lett.* **2005**, *30*, 1354–1356. [CrossRef] [PubMed]
6. Cuccia, D.J.; Bevilacqua, F.P.; Durkin, A.J.; Ayers, F.R.; Tromberg, B.J. Quantitation and mapping of tissue optical properties using modulated imaging. *J. Biomed. Opt.* **2009**, *14*, 024012. [CrossRef]
7. Gioux, S.; Mazhar, A.; Cuccia, D.J. Spatial frequency domain imaging in 2019: Principles, applications, and perspectives. *J. Biomed. Opt.* **2019**, *24*, 071613. [CrossRef]
8. Weber, J.R.; Durkin, A.J.; Tromberg, B.J.; Cuccia, D.J.; Johnson, W.R.; Wilson, D.W.; Bearman, G.H.; Hsu, M.; Lin, A.; Binder, D.K. Multispectral imaging of tissue absorption and scattering using spatial frequency domain imaging and a computed-tomography imaging spectrometer. *J. Biomed. Opt.* **2011**, *16*, 011015. [CrossRef]
9. Mazhar, A.; Dell, S.; Cuccia, D.J.; Gioux, S.; Durkin, A.J.; Frangioni, J.V.; Tromberg, B.J. Wavelength optimization for rapid chromophore mapping using spatial frequency domain imaging. *J. Biomed. Opt.* **2010**, *15*, 061716. [CrossRef]
10. MErfanzadeh, M.; Nandy, S.; Kumavor, P.D.; Zhu, Q. Low-cost compact multispectral spatial frequency domain imaging prototype for tissue characterization. *Biomed. Opt. Express* **2018**, *9*, 5503–5510. [CrossRef]
11. Wilson, R.H.; Nadeau, K.P.; Jaworski, F.B.; Rowland, R.; Nguyen, J.Q.M.; Crouzet, C.; Saager, R.B.; Choi, B.; Tromberg, B.J.; Durkin, A.J. Quantitative short-wave infrared multispectral imaging of in vivo tissue optical properties. *J. Biomed. Opt.* **2014**, *19*, 086011. [PubMed]
12. Vervandier, J.; Gioux, S. Single snapshot imaging of optical properties. *Biomed. Opt. Express* **2013**, *4*, 2938–2944. [CrossRef] [PubMed]
13. Van de Giessen, M.; Angelo, J.P.; Gioux, S. Real-time, profile-corrected single snapshot imaging of optical properties. *Biomed. Opt. Express* **2015**, *6*, 4051–4062. [CrossRef] [PubMed]
14. Aguénounon, E.; Smith, J.T.; Al-Taher, M.; Diana, M.; Intes, X.; Gioux, S. Real-time, wide-field and high-quality single snapshot imaging of optical properties with profile correction using deep learning. *Biomed. Opt. Express* **2020**, *11*, 5701–5716. [CrossRef] [PubMed]
15. Angelo, J.; Vargas, C.R.; Lee, B.T.; Bigio, I.J.; Gioux, S. Ultrafast optical property map generation using lookup tables. *J. Biomed. Opt.* **2016**, *21*, 110501. [CrossRef] [PubMed]
16. Chen, M.T.; Durr, N.J. Rapid tissue oxygenation mapping from snapshot structured-light images with adversarial deep learning. *J. Biomed. Opt.* **2020**, *25*, 112907. [CrossRef] [PubMed]
17. Zhao, Y.; Deng, Y.; Yue, S.; Wang, M.; Song, B.; Fan, Y. Direct mapping from diffuse reflectance to chromophore concentrations in multi-fx spatial frequency domain imaging (SFDI) with a deep residual network (DRN). *Biomed. Opt. Express* **2021**, *12*, 433–443. [CrossRef]
18. Erickson, T.A.; Mazhar, A.; Cuccia, D.J.; Durkin, A.J.; Tunnell, J.W. Lookup-table method for imaging optical properties with structured illumination beyond the diffusion theory regime. *J. Biomed. Opt.* **2010**, *15*, 036013. [CrossRef]
19. Hennessy, R.J.; Lim, S.L.; Markey, M.K.; Tunnell, J.W. Monte Carlo lookup table-based inverse model for extracting optical properties from tissue-simulating phantoms using diffuse reflectance spectroscopy. *J. Biomed. Opt.* **2013**, *18*, 037003. [CrossRef]
20. Zhong, X.; Wen, X.; Zhu, D. Lookup-table-based inverse model for human skin reflectance spectroscopy: Two-layered Monte Carlo simulations and experiments. *Opt. Express* **2014**, *22*, 1852–1864. [CrossRef]
21. Marti, D.; Aasbjerg, R.N.; Andersen, P.E.; Hansen, A.K. MCmatlab: An open-source, user-friendly, MATLAB-integrated three-dimensional Monte Carlo light transport solver with heat diffusion and tissue damage. *J. Biomed. Opt.* **2018**, *23*, 121622. [CrossRef] [PubMed]
22. Wang, L.; Jacques, S.L.; Zheng, L. MCML—Monte Carlo modeling of light transport in multi-layered tissues. *Comput. Methods Prog. Biomed.* **1995**, *47*, 131–146. [CrossRef]
23. Ren, N.; Liang, J.; Qu, X.; Li, J.; Lu, B.; Tian, J. GPU-based Monte Carlo simulation for light propagation in complex heterogeneous tissues. *Opt. Express* **2010**, *18*, 6811–6823. [CrossRef] [PubMed]
24. Fang, Q.; Boas, D.A. Monte Carlo simulation of photon migration in 3D turbid media accelerated by graphics processing units. *Opt. Express* **2009**, *17*, 20178–20190. [CrossRef] [PubMed]
25. Jacques, S.L. Optical properties of biological tissues: A review. *Phys. Med. Biol.* **2013**, *58*, R37. [CrossRef]
26. Clark, V.L.; Kruse, J.A. Clinical methods: The history, physical, and laboratory examinations. *JAMA* **1990**, *264*, 2808–2809.
27. Prahl, S. Optical Absorption of Hemoglobin. Available online: https://omlc.org/spectra/hemoglobin/ (accessed on 5 May 2021).
28. Gioux, S.; Mazhar, A.; Cuccia, D.J.; Durkin, A.J.; Tromberg, B.J.; Frangioni, J.V. Three-dimensional surface profile intensity correction for spatially modulated imaging. *J. Biomed. Opt.* **2009**, *14*, 034045. [CrossRef]